Calibration-less parallel imaging compressed sensing reconstruction based on OSCAR regularization

Loubna El Gueddari, Emilie Chouzenoux, Alexandre Vignaud, Philippe Ciuciu

Loubna El Gueddari, Emilie Chouzenoux, Alexandre Vignaud, Philippe Ciuciu. Calibration-less parallel imaging compressed sensing reconstruction based on OSCAR regularization. 2019. hal-02292372

HAL Id: hal-02292372

https://inria.hal.science/hal-02292372v1

Preprint submitted on 19 Sep 2019

Calibration-less parallel imaging compressed sensing reconstruction based on OSCAR regularization

Loubna El Gueddari, Emilie Chouzenoux, *Member IEEE,* Alexandre Vignaud, and Philippe Ciuciu, *Senior Member IEEE*

***Abstract*—Over the last decade, the combination of parallel imaging (PI) and compressed sensing (CS) in magnetic resonance imaging (MRI) has allowed to speed up acquisition while maintaining a good signal-to-noise ratio (SNR) for millimetric resolution. Self-calibrating techniques such as ℓ_1-ESPiRIT have emerged as a standard approach to estimate the coil sensitivity maps that are required at the reconstruction stage. Although straightforward in Cartesian acquisitions, these approaches become more computationally demanding in non-Cartesian scenarios especially for high resolution imaging (e.g. 500 μm in plane). Instead, calibration-less techniques no longer require this prior knowledge to perform multi-channel image reconstruction from undersampled k-space data. In this work, we introduce a new calibration-less PI-CS reconstruction method that is particularly suited to non-Cartesian data. It leverages structure sparsity of the multi-channel images in a wavelet transform domain while adapting to SNR inhomogeneities across receivers thanks to the OSCAR-norm regularization. Comparison and validation on 8 to 20-fold prospectively accelerated high-resolution ex-vivo human brain MRI data collected at 7 Tesla shows that the subbandwise OSCAR-norm regularization achieves the best trade-off between image quality and computational cost at the reconstructions stage compared to other tested versions (global, scalewise and pixelwise). This approach provides slight to moderate improvement over its state-of-the-art competitors (self-calibrating ℓ_1-ESPIRiT method and calibration-less AC-LORAKS and CaLM methods) in terms of closeness to the Cartesian reference magnitude image. Importantly, it also preserves much better phase information compared to other approaches.**

***Index Terms*—Compressed Sensing, Parallel MRI, non-Cartesian acquisition, Cluster norm, Proximal algorithms.**

I. INTRODUCTION

COMPPRESSED Sensing (CS) [1]–[3] has made a breakthrough in the MR community and now in clinics with recent FDA approval [4] as it provides ways to drastically shorten scan times especially when adopting non-Cartesian sampling schemes (radial, Propeller, spiral, Sparkling) [5]–[10] in the k-space. Non-Cartesian sampling patterns actually offer many advantages such as robustness to motion or better sampling efficiency [5]–[7], [9], [10]. For these reasons, non-Cartesian acquisitions make the usage of higher acceleration factors feasible as compared to Cartesian sampling, both in 2D and 3D imaging [10]. To maintain a high signal-to-noise ratio (SNR), CS k-space acquisition is usually combined with parallel imaging (PI), namely using multi-channel receiver coils [11] with no side effects.

The reconstruction of MR images from PI-CS k-space data has generated tens of contributions over the last decade. For instance, to cite a few in Cartesian acquisition scenarios, methods such as SAKE [12] or P-LORAKS [13], which are based on low-rank constraints in the k-space, have proved their efficiency to reconstruct MR images from multi-channel undersampled data with or without calibration lines (or points) in the k-space. However, as regards non-Cartesian acquisitions, MR image reconstruction is based on solving an inverse problem which often consists of minimizing an objective function where the data consistency term is balanced with a sparse prior (e.g., the ℓ_1-norm) over a given domain (e.g. the image gradient or a wavelet transform) [14], [15]. This prior enforces the image sparsity in this transformed domain. In that context, two types of reconstruction methods exist for non-Cartesian acquisitions: self-calibrating and calibration-less approaches.

Self-calibrating methods are based on the extraction of sensitivity maps that model the reception profile for each channel of a given coil. The sensitivity profiles are spatially smooth and can therefore be extracted from the k-space center which is usually densely sampled (along a variable density as required by CS). The extraction of sensitivity maps has been the matter of several works (cf [16]–[18]). Once these profiles estimated, they can be plugged in a SENSE-based formulation of the PI-CS reconstruction problem. Alternatively, one can jointly solve image reconstruction and coil sensitivity estimation as a blind bi-linear inverse problem [19], [20]. However, the computation cost of these methods gets really expensive for high-resolution imaging as one has to perform alternate minimization of the global objective function with respect to the image and sensitivity maps.

A. Related works

Instead of considering a 2-step procedure, calibration-less MR image reconstruction methods such as CalM (Calibration-less Multi coil) [21] came up with the idea of reconstructing one image per channel and enforcing some common prior knowledge between all images through for instance structured sparsity. Two different regularization terms have been used, group-sparsity in the wavelet domain [21], [22] and patch-based *local* low-rank in the image domain (CLEAR) [23].

L. El Gueddari and P. Ciuciu are both with NeuroSpin, CEA, Gif-sur-Yvette, 91191, France and Parietal, Inria, 91120 Palaiseau, France, whereas A. Vignaud is only affiliated with NeuroSpin (e-mails: firstname.lastname@cea.fr). E. Chouzenoux joined Centre Pour la Vision Numérique & Inria, Gif-sur-Yvette, 91191, France.

In terms of group-sparsity, the group-LASSO is likely the most convenient and efficient mixed-norm used for MR image reconstruction in the PI-CS framework [21], [22]. Although Chun *et al* demonstrate that promoting structured sparsity over the channels actually improves exact recovery guarantees in the PI-CS framework[1], the group-LASSO regularization is over-simplistic. It actually implements the idea that the same image sparsity in an appropriate transform domain (e.g. total variation, wavelets, frames) holds across all receiver channels. As such, it neglects the SNR fluctuations that exist between the multiple receivers of a given coil in any given region of the organ to be probed (e.g. the brain).

B. *Our contributions*

In this work, we propose a new calibration-less reconstruction method that goes beyond the group-LASSO penalty and takes advantage of the redundant information provided by each coil receiver. Our approach promotes structured sparsity across channels using a shrinkage and clustering algorithm namely the Octagonal Shrinkage and Clustering Algorithm for Regression (OSCAR) norm [24], [25]. OSCAR regularization actually relies on a combination of a ℓ_1 and pairwise ℓ_∞ norms that enables spatially clustering across receiver channels and thus implements an adaptive structured sparsity regularization. Practically, OSCAR may automatically uncover which receivers one must trust to get the highest image quality at the reconstruction stage. Interestingly, the OSCAR norm has a closed form proximity operator and as such is amenable in any nonsmooth proximity based optimization algorithm for image reconstruction purposes. In particular, we derive four versions of OSCAR regularization models and identify which one achieves the best trade-off between computational complexity and image quality for MR image reconstruction.

C. *Outline of the paper*

The rest of the paper is organized as follows. In Section II, we define the general formulation of the calibration-less MR image reconstruction problem. Then we detail the primal-dual optimization algorithm we use to solve this MR image reconstruction problem. In Section III, we recall the formulation of the OSCAR structured penalty. We then explore four variations of OSCAR-based regularization for the image reconstruction problem at hand and outline their differences for parallel computation purposes. In Section IV, we compare these implementations on real prospectively accelerated data sets collected at 7 Tesla using two non-Cartesian k-space readouts and various acceleration factors. In Section V, we discuss the pros and cons of the proposed approach in comparison with its competitors. Conclusions and perspectives are drawn in Section VI.

II. PROBLEM STATEMENT

Notation and definitions

In the following, we will denote vectors with bold letters, e.g. $\boldsymbol{v} = [v_1, \dots, v_p] \in \mathbb{C}^p$ a p-size complex-valued vector. Matrices are denoted using bold upper case letters (e.g., $\boldsymbol{A}$). The transpose of a matrix $\boldsymbol{A}$ is denoted by $\boldsymbol{A}^\top$, its Hermitian transpose by $\boldsymbol{A}^*$, its spectral norm by $|||\boldsymbol{A}|||$, and its Frobenius norm by $\|\boldsymbol{A}\|_2$.

Let $\Gamma_0(\mathbb{C}^p)$ the set of convex, proper, lower semi-continuous functions on $\mathbb{C}^p$ taking values on $\mathbb{R} \cup +\infty$. The proximity operator of a function $g \in \Gamma_0(\mathbb{C}^p)$ is defined as [26]: $\operatorname{prox}_g(\boldsymbol{z}) = \underset{\boldsymbol{v}\in\mathbb{C}^p}{\arg\min} \frac{1}{2}\|\boldsymbol{z}-\boldsymbol{v}\|^2 + g(\boldsymbol{v})$.

A. *General problem formulation*

Let us focus on the problem of MR image reconstruction in the multi-channel receiver coil setting. We set n the image resolution and $N = n^d$ the image size where d is the dimension[2], L the number of channels used to acquire the NMR signal and M the number of k-space measurements per channel, with $M < N$. For the sake of compactness, we denote the complete data set $\boldsymbol{Y} = [\boldsymbol{y}_1, \dots, \boldsymbol{y}_L] \in \mathbb{C}^{M\times L}$ which stacks $\boldsymbol{y}_\ell \in \mathbb{C}^M$ the k-space samples collected in the ℓ^{th} channel. Our goal is to recover L channel-specific complex-valued MR images that will be eventually combined to form a single full field-of-view (FOV) image. The way this combination is achieved will be clarified hereafter (especially for phase information).

In what follows, we do not take off-resonance effects and field inhomogeneities into account[3] and assume that the simple 2D discrete Fourier operator states for the forward model relating the k-space measurements to the unknown MR images. Actually, this operator heavily depends on the retained sampling strategy during the acquisition process. In the Cartesian sampling case, $\mathcal{F}_{\boldsymbol{M}} = \boldsymbol{MF}$, with $\boldsymbol{F}$ the 2D fast Fourier transform (FFT) and $\boldsymbol{M}$ the binary under-sampling mask defined over the discrete grid where each non-zero entry in $\boldsymbol{M}$ selects a row in $\boldsymbol{F}$. In non-Cartesian settings, $\boldsymbol{F}$ refers to non-equispaced or nonuniform FFT [28], [29] and $\boldsymbol{M}$ stands for the continuous support of the measurements in k-space. Each channel measurement $\boldsymbol{y}_\ell$, with $\ell \in \{1, \dots, L\}$, is furthermore affected by an additive circular complex i.i.d. zero-mean Gaussian noise of variance σ_ℓ^2.

The goal is then to retrieve, from the noisy under-sampled data $(\boldsymbol{y}_\ell)_{1\le\ell\le L}$, L MR images stacked in $\boldsymbol{X} = [\boldsymbol{x}_1, \dots, \boldsymbol{x}_L] \in \mathbb{C}^{N\times L}$ such that each $\boldsymbol{x}_\ell \in \mathbb{C}^N$ is associated with the $\ell^{\textbf{th}}$ channel of the phased array coil. We propose to solve this ill-posed inverse problem by adopting a variational penalized formulation, which consists of minimizing the following criterion:

$$\widehat{\boldsymbol{X}} = \underset{\boldsymbol{X}\in\mathbb{C}^{N\times L}}{\arg\min} \Big\{ \sum_{\ell=1}^{L} \frac{1}{2\sigma_\ell^2} \|\mathcal{F}_{\boldsymbol{M}}\boldsymbol{x}_\ell - \boldsymbol{y}_\ell\|_2^2 + g(\boldsymbol{\Psi X}) \Big\}. \quad (1)$$

Hereabove, $g \in \Gamma_0(\mathbb{C}^{N_\Psi\times L})$ is a regularization function composed with a linear operator $\boldsymbol{\Psi} \in \mathbb{C}^{N_\Psi\times N}$, with the aim to enforce sparsity of the solution within a given multiscale decomposition (e.g., wavelet transform). This formulation enables the use of over-complete dictionaries [30], [31]. We will

---

[1] One can lower the number of k-space samples to get perfect image reconstruction in the noise-free case as multiple k-space are collected over the receiver channels.

[2] In 2D imaging $d = 2$, whereas in 3D imaging $d = 3$.

[3] see for instance [27] to handle fast conjugate phase reconstruction in the single channel case.

assume that $\boldsymbol{\Psi}$ decomposes the stack of L images $\boldsymbol{X} \in \mathbb{C}^{N\times L}$ into a stack of coefficients $\boldsymbol{\Psi X} \in \mathbb{C}^{N_\Psi\times L}$ with C scales. Each scale $c \in \{1,\dots,C\}$ is composed of S_c sub-bands. Each sub-band $s \in \{1,\dots,S_c\}$ has $K_{s(c)}$ coefficients, so that finally $N_\Psi = \sum_{c=1}^{C}\sum_{s=1}^{S_c} K_{s(c)}$. For the sake of simplicity, in what follows we assume that $S_c = S, \forall c$ and $K_{s(c)} = K_c \, \forall s$. As an example, for $n\times n$ images using decimated Wavelet transform, we would have $K_{s(c)} = n/2^c \times n/2^c$ and $S_c = 3$ for all scales except for the last one where $S_c = 4$. Moreover, the k^{th}-coefficient in the s^{th}-sub-band of the c^{th}-scale for the ℓ^{th}-coil will be denoted as $z_{csk\ell}$. Vector $\boldsymbol{z}_{csk,:} \in \mathbb{C}^L$ gathers the multi-channel coefficients $(z_{csk\ell})_{1\le\ell\le L}$ at position k, sub-band s and c-scale. Similarly, the larger vector $\boldsymbol{z}_{cs,:}$ stacks the multi-position and multi-channel coefficients $(z_{csk\ell})_{1\le k\le K_c, 1\le\ell\le L}$ at a given sub-band s of scale c. Last, vector $\boldsymbol{z}_{c,:}$ stacks the multi-band multi-position and multi-channel coefficients $(z_{csk\ell})_{1\le s\le S, 1\le k\le K_c, 1\le\ell\le L}$ at a given scale c.

The resolution of Problem (1) delivers L channel images $(\widehat{\boldsymbol{x}}_\ell)_{1\le\ell\le L}$, stacked in $\widehat{\boldsymbol{X}}$. Once Problem (1) is solved, all coil-specific MR images $(\widehat{\boldsymbol{x}}_\ell)_{1\le\ell\le L}$ are combined using the square-root of the sum-of-squares (sSOS), $\widehat{\boldsymbol{x}}_{\text{sSOS}} = \sqrt{\sum_{\ell=1}^{L} \|\widehat{\boldsymbol{x}}_\ell\|_2^2}$, to form a single *magnitude* image as usually done in parallel imaging [11]. The virtual coil method is also used to combine *phase information* across all channels [32] and get $\widehat{\boldsymbol{x}}_{s\angle}$. Let us remark that Problem (1) is called *calibration-less*. It is in contrast with Sensitivity Encoding (SENSE) formulation which aims at directly reconstructing a single full FOV image $\boldsymbol{x} \in \mathbb{C}^N$ from multi-channel data $(\boldsymbol{y}_\ell)_{1\le\ell\le L}$, assuming the extra knowledge of sensitivity maps $(\boldsymbol{S}_\ell)_{1\le\ell\le L}$ such that $\boldsymbol{x}_\ell = \boldsymbol{S}_\ell \boldsymbol{x}$.

In what follows, we propose an efficient proximal optimization method to solve Problem (1).

B. Primal-dual optimization algorithm

Problem (1) amounts to solve

$$\widehat{\boldsymbol{X}} \in \underset{\boldsymbol{X}\in\mathbb{C}^{N\times L}}{\operatorname{argmin}} \left[f(\boldsymbol{X}) + g(\boldsymbol{\Psi X})\right]. \tag{2}$$

where we denote:

$$(\forall \boldsymbol{X} \in \mathbb{C}^{N\times L}) \quad f(\boldsymbol{X}) = \sum_{\ell=1}^{L} \|\mathcal{F}_{\boldsymbol{M}}\boldsymbol{x}_\ell - \boldsymbol{y}_\ell\|_2^2/(2\sigma_\ell^2). \tag{3}$$

Function f belongs to $\Gamma_0(\mathbb{C}^{N\times L})$ and it is β-Lipschitz differentiable i.e.:

$$(\forall \boldsymbol{X}, \boldsymbol{X}' \in \mathbb{C}^{N\times L}), \quad \|\nabla f(\boldsymbol{X}) - \nabla f(\boldsymbol{X}')\|_2 \le \beta\|\boldsymbol{X} - \boldsymbol{X}'\|_2, \tag{4}$$

with $\beta = \sum_{l=1}^{L} (\sigma_\ell^2)^{-1} |||\mathcal{F}_{\boldsymbol{M}}|||^2$. Moreover, function g belongs to $\Gamma_0(\mathbb{C}^{N\times L})$. We thus propose to make use of the primal-dual proximal algorithm from Condat-Vú [33], [34], which leads to Algorithm 1.

According to [33, Theorem 3.1], the sequence $(\boldsymbol{X}_k)_{k\in\mathbb{N}}$ generated by Algorithm 1 weakly converges to a solution of Problem (2) as soon as $\frac{1}{\tau} - \kappa|||\boldsymbol{\Psi}|||^2 \ge \frac{\beta}{2}$. In practice, the hyper-parameters of this algorithm are set as follows: $\tau := \frac{1}{\beta}$, $\kappa := \frac{\beta}{2|||\boldsymbol{\Psi}|||^2}$. Note that when $\boldsymbol{\Psi}$ defines a basis, we get $|||\boldsymbol{\Psi}||| = 1$. The main advantage of Algorithm 1 is that it does not involve the computation of $\text{prox}_{g\circ\boldsymbol{\Psi}}$. The latter does not usually have closed form, in particular when $\boldsymbol{\Psi}$ is overcomplete (e.g. undecimated wavelet transform), and would require the use of an inner iterative solver [35].

Algorithm 1: Condat-Vú algorithm

```
Set $\tau > 0$, $\kappa > 0$, $\boldsymbol{X}_0 \in \mathbb{C}^{N\times L}$, $\boldsymbol{Z}_0 \in \mathbb{C}^{N_\Psi\times L}$;
for $t = 0,\dots,T$ do
    $\boldsymbol{X}_{t+1} := \boldsymbol{X}_t - \tau\left(\nabla f(\boldsymbol{X}_t) + \boldsymbol{\Psi}^*\boldsymbol{Z}_t\right)$;
    $\boldsymbol{W}_{t+1} := \boldsymbol{Z}_t + \kappa\,\boldsymbol{\Psi}\left(2\boldsymbol{X}_{t+1} - \boldsymbol{X}_t\right)$;
    $\boldsymbol{Z}_{t+1} := \boldsymbol{W}_{t+1} - \kappa\ \text{prox}_{g/\kappa}\left(\frac{\boldsymbol{W}_{t+1}}{\kappa}\right)$;
end
```

III. OCTAGONAL SHRINKAGE AND CLUSTERING ALGORITHM FOR REGRESSION

A. OSCAR regularizer

1) Definition: Let $\boldsymbol{z} \in \mathbb{C}^p$ with $p \ge 1$. We introduce the magnitude sorting operator $S_p : \mathbb{C}^p \to \mathbb{C}^p$ such that vector $S_p(\boldsymbol{z}) = (S_p(\boldsymbol{z})_j)_{1\le j\le p}$ contains the p entries of $\boldsymbol{z}$ sorted in decreasing order in magnitude, i.e., such that

$$|S_p(\boldsymbol{z})_1| \ge |S_p(\boldsymbol{z})_2| \ge \cdots \ge |S_p(\boldsymbol{z})_p|. \tag{5}$$

Then, OSCAR norm is defined as follows:

$$\Omega_{\lambda,\gamma}(\boldsymbol{z}) = \lambda\|\boldsymbol{z}\|_1 + \gamma \sum_{1\le j<k\le p} \max(|z_j|, |z_k|). \tag{6}$$

with λ, γ positive hyper-parameters. The ℓ_1-norm term in $\Omega_{\lambda,\gamma}$ promotes the sparsity of $\boldsymbol{z}$ while the second term, corresponding to a pairwise ℓ_∞-norm, encourages the equality of each entry pair in $\boldsymbol{z}$. As pointed out in [36, Sec. II. A.], OSCAR norm has a closed relation with the Ordered Weighted ℓ_1 (OWL) norm defined below:

$$\Theta_{\boldsymbol{w}}(\boldsymbol{z}) = \sum_{j=1}^{p} w_j |S_p(\boldsymbol{z})_j|. \tag{7}$$

with $\boldsymbol{w} \in \mathbb{R}_+^p$ a vector of hyper-parameters such that $w_1 \ge \cdots \ge w_p \ge 0$. More precisely, OWL and OSCAR become equivalent if one sets the OWL weights $w_j = \lambda + \gamma(p - j)$ for $j = 1,\dots,p$.

2) Proximity operator: Let $\boldsymbol{z} \in \mathbb{C}^p$. If $\boldsymbol{z}$ is equal to zero, then the proximity operator of the OWL norm at $\boldsymbol{z}$ is also equal to zero. Otherwise, it can be efficiently computed thanks to the following algorithm as shown in [36, Sec.III A]:

Algorithm 2: Proximity operator of the OWL norm.

```
Input: $\boldsymbol{z} \in \mathbb{C}^p/\{0\}$, $\boldsymbol{w} \in \mathbb{R}^p$ ;
$\boldsymbol{n} = |\boldsymbol{z}|/\boldsymbol{z}$;
Let $\boldsymbol{P} \in \mathbb{R}^{p\times p}$ s.t. $S_p(\boldsymbol{n}) = \boldsymbol{P}\boldsymbol{n}$;
Return $\text{prox}_{\Theta_{\boldsymbol{w}}}(\boldsymbol{z}) = \boldsymbol{n} \odot \boldsymbol{P}^\top \text{PAV}(S_p(\boldsymbol{n}) - \boldsymbol{w})$;
```

Hereabove, PAV refers to the Pool Adjacent Violator Algorithm [37] and $\odot$ to the Hadamard product (i.e. element-wise multiplication). The proximity operator of OSCAR can thus be easily deduced by setting the appropriate value for $\boldsymbol{w}$ mentioned above, so that OSCAR and OWL match together.

B. OSCAR-based image reconstruction

Data acquired with a multi-channel receiver coil are highly correlated since the associated k-space samples are collected using the same readout, but with channel-specific sensitivity profiles. Sparsity-based inference in the highly correlated setup has been a well studied topic in data science [38], [39]. In particular, it was pointed out that the ℓ_1 regularization may failed when multiple block of variables are highly correlated as the solution tends to select one of those blocks. OSCAR regularization has been specifically designed to perform both shrinkage and variable selection [24], [25], [36]. It is thus well suited for PI-CS MR image reconstruction from highly correlated data.

In what follows, we propose four choices for function g in Problem (2) relying on OSCAR norm, with the aim to perform efficient calibration-less MR image reconstruction. The main difference lies in the way the OSCAR norm is applied to the sparsifying decomposition $\boldsymbol{Z} = \boldsymbol{\Psi X} = [\boldsymbol{z}_1 \dots \boldsymbol{z}_\ell] \in \mathbb{C}^{N_\Psi \times L}$ of the muti-channel image $\boldsymbol{X} = [\boldsymbol{x}_1 \dots \boldsymbol{x}_\ell] \in \mathbb{C}^{N \times L}$.

1) Global OSCAR regularization: The most straightforward way to implement OSCAR-based regularization consists of flattening all wavelet coefficients and thus discarding the multiscale and multi-channel structure (e.g. in scales, sub-bands, coefficients and channels) of $\boldsymbol{Z}$. For that reason, we call this version global OSCAR (g-OSCAR) regularization. The wavelet coefficients are stacked together, leading to a single but large vector with entries $(z_j)_{1 \le j \le LN_\Psi}$, where we remind that $N_\Psi = S\sum_{c=1}^{C} K_c$ and $N_\Psi = N$ when $\boldsymbol{\Psi}$ is orthogonal. The g-OSCAR regularizer then reads:

$$\begin{aligned} g_{\text{g-OSCAR}}(\boldsymbol{Z}) &= \Omega_{\lambda,\gamma}(\boldsymbol{Z}) \\ &= \sum_{j=1}^{LN_\Psi} \lambda |z_j| + \gamma \sum_{1 \le j < k \le LN_\Psi} \max\{|z_j|, |z_k|\} \\ &= \sum_{j=1}^{LN_\Psi} \left(\lambda + \gamma(LN_\Psi - j)\right) |S_{LN_\Psi}(\boldsymbol{z})_j| \,. \end{aligned} \tag{8}$$

2) Scalewise OSCAR regularization: We now propose a scalewise formulation, where OSCAR norm is applied to each specific scale c of the wavelet decomposition, hence to each vector $\boldsymbol{z}_{c,:}$ separately. This leads to the so-called s-OSCAR regularizer:

$$\begin{aligned} g_{\text{s-OSCAR}}(\boldsymbol{Z}) &= \sum_{c=1}^{C} \Omega_{\lambda,\gamma}(\boldsymbol{z}_{c,:}) \\ &= \sum_{c=1}^{C} \sum_{j=1}^{LSK_c} \left(\lambda + \gamma(LSK_c - j)\right) |S_{LSK_c}(\boldsymbol{z}_{c,:})_j| \,, \end{aligned} \tag{9}$$

where vector $\boldsymbol{z}_{c,:}$ gathers the LSK_c wavelet coefficients across all channels in a specific scale $c \in \{1, \dots, C\}$. In that way, the wavelet coefficients can be clustered together regardless the sub-band they belong to, their position and their channel dependence. Thus, C sorting operations are required, each of them involving LSK_c parameters. As the s-OSCAR regularization is separable by scales, the computation of its proximity operator can be performed efficiently using parallelization over scales.

3) Sub-bandwise OSCAR regularization: The present formulation applies OSCAR regularization to each specific sub-band of the wavelet decomposition, hence to each vector $\boldsymbol{z}_{cs,:}$ separately. We then obtain the b-OSCAR regularizer:

$$\begin{aligned} g_{\text{b-OSCAR}}(\boldsymbol{Z}) &= \sum_{c=1}^{C} \sum_{s=1}^{S} \Omega_{\lambda,\gamma}(\boldsymbol{z}_{cs,:}) \\ &= \sum_{c=1}^{C} \sum_{s=1}^{S} \sum_{j=1}^{K_c L} \left(\lambda + \gamma(K_c L - j)\right) |S_{K_c L}(\boldsymbol{z}_{cs,:})_j| \,, \end{aligned} \tag{10}$$

where vector $\boldsymbol{z}_{cs,:}$ gathers the $K_c L$ wavelet coefficients across all channels in a given subband s of scale c. Here again, the separability of the regularizer can be exploited for an efficient implementation of the proximity operator.

4) Coefficient-wise OSCAR regularization: Finally we propose to apply OSCAR norm to each wavelet coefficient separately and thus to each vector $\boldsymbol{z}_{csk,:}$, leading to c-OSCAR regularization:

$$\begin{aligned} g_{\text{c-OSCAR}}(\boldsymbol{Z}) &= \sum_{c=1}^{C} \sum_{s=1}^{S} \sum_{k=1}^{K_c} \Omega_{\lambda,\gamma}(\boldsymbol{z}_{csk,:}) \\ &= \sum_{c=1}^{C} \sum_{s=1}^{S} \sum_{k=1}^{K_c} \sum_{\ell=1}^{L} \left(\lambda + \gamma(L - \ell)\right) |S_L(\boldsymbol{z}_{csk,:})_\ell| \,, \end{aligned} \tag{11}$$

where vector $\boldsymbol{z}_{csk,:}$ gathers the L wavelet coefficients across all channels for coefficient k in sub-band s of scale c. This formulation is the closest to the usual application of the group-LASSO structured sparsity penalty [22] as it operates separately on each pixel in the transformed domain. However, instead of implicitly assuming constant noise level over all channels by taking the ℓ_2-norm, the c-OSCAR regularization allows to weight these channels differently thanks to the sorting step and to adapt regularization to space-varying noise levels.

IV. EXPERIMENTS & RESULTS

To assess the quality of the proposed calibration-less MR image reconstruction method, we proceed in two steps. First, we compare the four OSCAR-based formulations, described in Section III, in terms of image quality and computational complexity. Second, we provide comparisons with state-of-the-art methods, namely CaLM [21], ℓ_1-ESPIRiT [17] and AC-LORAKS [13], [40]. Hereafter, we describe the experimental setup we used for validation purposes.

Importantly, it should be noted that prospective non-Cartesian acquisitions have been implemented, as such type of readouts allows higher acceleration factors than Cartesian ones while preserving image quality. CS reconstruction methods are barely compared in non-Cartesian imaging and even less in prospective acquisition scenarios. A great advantage of the proposed calibration-less approach is to enable such type of comparisons in an extensive manner.

A. Experimental setup

All numerical experiments were conducted on 2D k-space data even though the proposed framework could be extended to 3D imaging quite directly. Hence, we only report results on slices.

1) Prospective non-Cartesian acquisition: We consider the reconstruction of an ex-vivo human brain with a in plane resolution of 0.39×0.39 mm^2 for different acquisition schemes prospectively acquired on a 7T MR system (Magnetom Siemens Healthineers, Erlangen, Germany) using a $L = 32$-channel coil (Nova Medical Inc., Washington, MA, USA). Spiral trajectories [6] were generated for different undersampling factors as detailed in Tab. I. More advanced sampling schemes were also designed using Sparkling (Spreading Projection Algorithm for Rapid K-space samplING) [8], [10]. Sparkling method generates physically plausible trajectories with improved robustness to gradient imperfections and is less prone to off-resonance artifacts as shown in [10]. The resulting sampling schemes are known to reach higher image quality for a given scan time, compared to state-of-the art trajectories (e.g spiral or radial). The acquisition parameters were set as follows: FOV $= 200 \times 200$ mm^2, TR $=$ 550 ms (for 11 slices), TE $=$ 30 ms, BW $=$ 100 kHz, $T_{\rm obs} = 30.72$ ms (long readout) and FA=25° with in-plane resolution of 390 μm and slice thickness of 3 mm. In Tab. I), we summarized the different data sets we considered by varying the undersampling or acceleration factor for both Sparkling and Spiral readouts. Fully sampled Cartesian measurements were acquired and reconstructed into an image which will serve as ground truth using the same sequence parameters (matrix size: $N = 512 \times 512$ or $n = 512$).

TABLE I
ACQUISITION PARAMETERS USED FOR PROSPECTIVE CS EX VIVO T_2^* ACQUISITION ON THE SAME HUMAN BRAIN.

Idx	Sampling scheme	Acceleration Factor	Undersampling Factor
1.	Sparkling, cf Fig. 1(a)	8	1.3
2.		10	1.7
3.		12	2
4.		15	2.5
5.		20	3.3
6.	Spiral, cf Fig. 1(b)	8	1.3
7.		10	1.7
8.		12	2
9.		15	2.5
10.		20	3.3

To understand the difference between acceleration factor (AF) in time and undersampling factor (UF) in number of measurements, one has to recall the following relations: AF $= n/n_c$ where n_c is the number of shots. For instance, we used $n = 512$ and varied n_c between 64 down to 26 corresponding to acceleration in time from 8 to 20, as reported in Tab. I. In the same time, we implemented oversampling along each shot ($n_s = 3,072$ samples per shot) as usually done in non-radial non-Cartesian trajectories, hence the undersampling factor defined as UF $= N/M$ with $M = n_c \times n_s$ varied in a more limited range from 1.3 to 3.3.

Fig. 1 shows the in/out[4] Sparkling and spiral multi-shot trajectories played by the headonly gradient system (AC84) installed on the 7 MR system for an acceleration factor of 20.

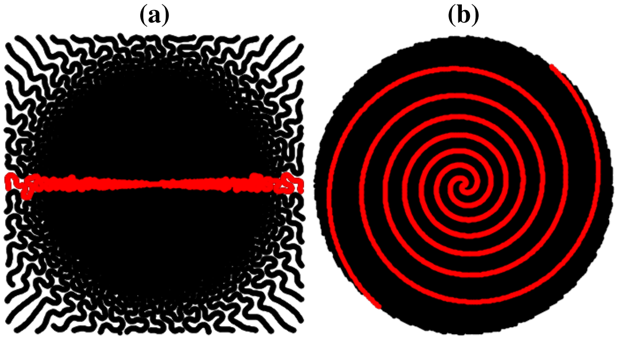

Fig. 1. Non-Cartesian in-out variable density sampling schemes used in prospective CS at 7 Tesla. **(a)**: 20-fold accelerated-in-time Sparkling trajectories (26 shots). **(b)**: 20-fold accelerated-in-time spiral trajectories with the same number of shots and measurements as Sparkling. For details about their generation, see [10] for Sparkling and [6] for spiral imaging. The trace of a single in-out shot is highlighted in red.

B. Reconstruction parameters

Algorithm 1 was run until $T = 150$ iterations, which appears sufficient for reaching convergence of the iterates. Moreover, we used for $\boldsymbol{\Psi}$ a Daubechies 4 orthogonal wavelet transform (OWT) with $C = 4$ decomposition scales (i.e., $N_\Psi = N$). Note that MR image quality can be improved using redundant multiscale transforms (e.g. undecimated bi-orthogonal wavelet transforms or curvelets as shown in [41]) but this kind of decomposition significantly increases the memory load and computation time of the overall algorithm.

In Tab. II, we summarize the numerical complexity of the four OSCAR-norm regularizations, the computing time required for evaluating both their proximity operator and running one full iteration of Algorithm 1. The parallelization of the proximity step involved in the OSCAR-norm regularizations was performed using `joblib`, a Python package that allows embarrassingly parallel computations. The number of parallel threads that were used is indicated in Tab. II. All experiments were run on a machine with 128 GB of RAM and an 8-core (2.40 GHz) Intel Xeon E5-2630 v3 Processor.

From the computational point of view, the b-OSCAR approach seems the most appealing. Indeed, its proximity operator can be computed faster (see Tab. II) since the number of threads (16 in this case) matches the number of wavelet sub-bands for this decomposition. This yields an optimal parallelization scheme.

The overall algorithm was implemented in `PySAP`[5], an open source software written in Python and dedicated to sparse multiscale representation and analysis of images.

The hyper-parameters (λ, γ) were set using a grid search procedure so as to maximize the SSIM [42] score of the combined magnitude image $\widehat{\boldsymbol{x}}_{\rm sSOS}$. We provide in Fig. 2**(a)** an illustration of the robustness of the setting of (λ, γ) by showing that image quality (SSIM score) reaches a plateau

---

[4] Start from one border of k-space, go to the center and move to the opposite border.

[5] `https://github.com/CEA-COSMIC/pysap`

TABLE II
NUMERICAL COMPLEXITY AND PARALLELIZATION CAPACITY OF OSCAR-NORM REGULARIZATIONS USING DAUB. 4 OWT AND $(N, C, L) = (512^2, 4, 32)$ FOR MRI RECONSTRUCTION.

	Prox. numerical complexity	Comput. time per prox. (s)	Paral.	Iter. (s)
g-OSCAR	$O(LN_\Psi \log(LN_\Psi))$	3.47	N.A.	8.97
s-OSCAR	$O(\sum_{c=1}^{C} LK_cS_c \log(LS_cK_c))$	3.16	C	12.17
b-OSCAR	$O(\sum_{c=1}^{C} LK_cS_c \log(LK_c))$	2.61	CS	11.20
c-OSCAR	$O(N_\Psi L \log L)$	42.05	N_Ψ	47.55

for a large range of parameters with a maximal and minimal values respectively reaching 0.901 and 0.822. In Fig. 2**(b)**, we replicated the same analysis using the pSNR score for the same data set (20-fold accelerated Sparkling). We found similar optimal values around $(\lambda, \gamma) = (10^{-6.5}, 10^{-10.5})$. In this case, the image quality remains quite constant as λ fluctuates and γ is fixed with a maximal and minimal values reaching respectively 29.77 dB and 27.33 dB. However, the pSNR value significantly drops off when γ departs from its optimal setting. Given this lack of robustness, all results presented in the following were obtained using the SSIM score as target metric for setting (λ, γ). This approach was retained both for OSCAR-norm regularization but also for its competitors (e.g. ℓ_1-ESPIRIT, CaLM). The combined phase images $\widehat{\boldsymbol{x}}_{s\angle}$ shown at the bottom of Figs. 3-4 have not been unwrapped. Magnitude and phase images were thus compared separately.

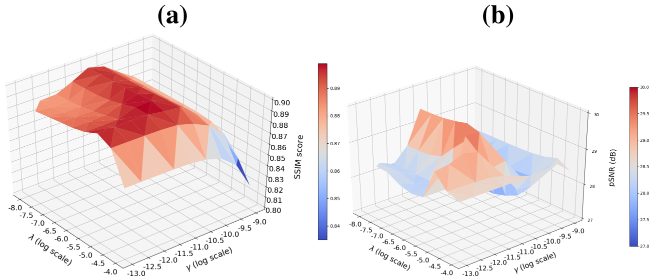

Fig. 2. Map of **(a)** SSIM **(b)** pSNR score as a function of hyperparameters (λ, γ) involved in OSCAR-band (b-OSCAR) regularization using 20-fold accelerated Sparkling sampling scheme.

C. Results

First, the four OSCAR-norm regularizations were compared on the 10 different data sets summarized in Tab. I. Second, we extended this comparison to other state-of-the-art methods including calibration-less (CaLM [21], AC-LORAKS [44]) and self-calibrating ones (ℓ_1-ESPIRiT [17]). AC-LORAKS was preferred to P-LORAKS [13] as it is less demanding from a computational viewpoint.

1) Comparison of OSCAR-norm regularizations: Tab. III summarizes the image quality scores (SSIM, pSNR and NRMSE) of the four versions of OSCAR-norm regularization. Over the five Sparkling data sets, the best scores were obtained by the b- and c-OSCAR versions, although the differences in terms of SSIM scores with other versions remain pretty small. The slight gain can be explained by the fact that g- and s-OSCAR versions mix up different oriented details or resolution information together. We observed that coefficient-wise regularization performs slightly better than subbandwise one as the acceleration factor increases. This suggests that localized regularization in space preserves much better the image details in highly accelerated acquisitions. Similar findings were replicated on an ex-vivo baboon brain (results not shown). Over the five spiral data sets, the best SSIM scores are yielded in the vast majority of cases by the b- and c-OSCAR regularizations illustrating the consistency between the two readout scenarios. When comparing the two acquisition strategies, spiral imaging seems to provide better SSIM scores especially for higher acceleration factors. However, this quantitative assessment is not strictly consistent with image quality perception. In Figs. 3-4, we actually report the results for the 20-fold accelerated Sparkling and spiral scans: Spiral MR images are contaminated by severe off-resonance artifacts, see for instance the blue arrows reported in Fig. 4 whereas Sparkling ones are not (see Fig. 3). This results from the much better point spread function (PSF) associated with Sparkling sampling as shown in [10].

2) Comparison with other reconstruction methods: Tab. IV summarizes the quantitative performances (SSIM, pSNR and NRMSE) of competing reconstruction approaches, computed over the magnitude images. These competitors embed i) zero-order inverse NFFT (i.e. least squares solution in Eq. (1)), two calibration-less techniques ii) CaLM which implements a group-LASSO alternative to c-OSCAR penalization and iii) AC-LORAKS, and the state-of-the-art self-calibrating method iv) ℓ_1-ESPIRiT. As in Sparkling and spiral acquisitions the k-space center is heavily sampled, ℓ_1-ESPIRiT performs well for extracting the sensitivity maps which are then used for solving the ℓ_1-norm regularized CS-SENSE reconstruction problem. The bottleneck in AC-LORAKS lies in the gridding operation required to project the non-Cartesian samples onto the Cartesian grid. This step degrades image quality and demonstrates that AC-LORAKS may not be really compliant with non-Cartesian sampling.

In terms of SSIM and pSNR scores, CaLM regularization outperforms all other techniques. However, CaLM performances remain below or similar to those of OSCAR, whether it is the subbandwise or coefficientwise version. This confirms that extending the group-LASSO penalization using a pairwise ℓ_∞-norm between channels instead of the global the ℓ_2-norm may be beneficial to account for varying SNR across channels. We also noticed that in Sparkling acquisitions the regularization systematically improved all image quality scores, whereas in spiral imaging the pSNR/NRMSE values were better for the zero-order solution (inverse FT). As the regularization parameters were optimally set wrt the SSIM score, CaLM regularization actually demonstrated slightly improved performance in terms of SSSIM.

Importantly, in Figs. 3-4 we show that calibration-less reconstruction techniques such as OSCAR and CaLM better preserve phase information in comparison with ℓ_1-ESPIRiT and AC-LORAKS. As there is no sensitivity map extraction in calibration-less approaches, any phase-related error (e.g. shift)

TABLE III

COMPARISON OF OSCAR-NORM REGULARIZATIONS WITH HYPER-PARAMETERS SET TO MAXIMIZE THE SSIM SCORE. BEST IMAGE QUALITY METRICS COMPUTED PER ROW APPEAR IN BOLD FONT. THREE SCORES ARE THUS OUTLINED ON EACH ROW, SOMETIMES MORE IN CASE OF EQUALITY.

Idx	g-OSCAR			s-OSCAR			b-OSCAR			c-OSCAR		
	SSIM	pSNR	NRMSE	SSIM	pSNR	NRMSE	SSIM	pSNR	NRMSE	SSIM	pSNR	NRMSE
1.	0.923	30.52	0.1471	0.925	31.66	0.1290	**0.926**	**31.68**	**0.1287**	0.924	30.96	0.1398
2.	0.920	29.21	0.1711	0.921	29.62	0.1632	**0.922**	**30.28**	**0.1512**	**0.922**	29.59	0.1636
3.	0.916	28.81	0.1792	**0.918**	28.40	0.1878	**0.918**	**29.78**	**0.1602**	**0.918**	29.33	0.1688
4.	0.912	29.28	0.1700	0.912	29.05	0.1742	**0.913**	29.52	0.1650	**0.913**	**29.66**	**0.1624**
5.	0.899	29.12	0.1728	0.896	28.35	0.1889	0.899	29.52	0.1650	**0.901**	**29.77**	**0.1604**
6.	0.932	30.12	0.1540	0.931	**30.70**	**0.1440**	**0.933**	30.36	0.1498	**0.933**	30.66	0.1447
7.	0.928	29.76	0.1606	0.927	**30.50**	0.1474	**0.928**	29.92	**0.1576**	**0.928**	29.92	0.1577
8.	0.922	29.35	0.1683	**0.923**	29.74	0.1609	0.921	31.22	0.1358	0.922	**31.50**	**0.1319**
9.	0.920	29.18	0.1715	0.920	29.89	0.1581	0.919	**30.22**	**0.1522**	**0.921**	29.72	0.1613
10.	**0.916**	29.72	0.1614	0.914	29.40	0.1673	0.915	**29.84**	**0.1592**	**0.916**	29.66	0.1623

TABLE IV

COMPARISON OF STATE-OF-THE-ART METHODS FOR NON-CARTESIAN PI-CS RECONSTRUCTION USING EITHER A CALIBRATION-LESS OR SELF-CALIBRATING APPROACH. BEST IMAGE QUALITY METRICS COMPUTED PER ROW APPEAR IN BOLD FONT.

Idx	No regularization			CaLM			ℓ_1-ESPIRiT			AC-LORAKS		
	SSIM	pSNR	NRMSE	SSIM	pSNR	NRMSE	SSIM	pSNR	NRMSE	SSIM	pSNR	NRMSE
1.	0.908	**30.57**	**0.1463**	**0.924**	30.51	0.1473	0.911	27.82	0.1946	0.894	26.09	0.2375
2.	0.906	29.19	0.1715	**0.921**	**29.54**	**0.1647**	0.906	26.58	0.2246	0.897	26.23	0.2340
3.	0.902	28.89	0.1774	**0.917**	**29.05**	**0.1741**	0.904	27.17	0.2099	0.893	26.25	0.2333
4.	0.894	28.39	0.1880	**0.912**	**28.87**	**0.1778**	0.900	26.29	0.2323	0.884	25.94	0.2418
5.	0.884	28.25	0.1911	**0.897**	**28.59**	**0.1836**	0.885	26.48	0.2272	0.753	25.52	0.2536
6.	0.927	**31.55**	**0.1307**	**0.932**	30.95	0.1400	0.927	26.37	0.2300	0.921	27.55	0.2008
7.	0.925	**31.64**	**0.1293**	**0.928**	29.87	0.1585	0.925	26.07	0.2382	0.921	27.54	0.2010
8.	0.922	**31.47**	**0.1391**	**0.922**	29.55	0.1645	0.922	26.27	0.2328	0.919	27.23	0.2084
9.	0.916	**29.86**	**0.1588**	**0.920**	29.21	0.1711	0.916	26.33	0.2311	0.911	26.67	0.2221
10.	0.911	**29.79**	**0.1599**	**0.915**	29.52	0.1650	0.910	25.86	0.2439	0.902	26.23	0.2338

in that step does not propagate during the image reconstruction itself. Such artifacts are particularly visible in ℓ_1-ESPIRiT for spiral imaging (see red arrows in Fig. 4). Phase images based on AC-LORAKS are also corrupted by artifacts that may be due to the gridding operation, especially for Sparkling imaging (see red arrows in Fig. 3).

V. DISCUSSION

Non-Cartesian trajectories have been used for many different applications and have recently met a renew of interest to accelerate scan time. However, in the PI-CS context most of reconstruction methods are more suited for Cartesian acquisitions than for non-Cartesian ones. This is especially the case of calibration-less techniques.

Importantly the proposed method has theoretical guarantees of convergence and is made of fully interpretable steps which makes it more reliable and robust to small perturbations than recent deep learning approaches [45], [46] proposed for medical image reconstruction [47]. Indeed, we formulated PI-CS image reconstruction as an inverse ill-posed problem and made use of nonuniform FFT for dealing with non-Cartesian trajectories and OSCAR-norm penalty for regularization purposes. We instantiated four different versions of OSCAR-norm regularization with different compromises between numerical complexity and modeling accuracy. Then, we relied on state-of-the-art convex nonsmooth optimization tools, namely the Condat-Vù algorithm with sound convergence properties to compute the global minimizer of the derived cost function. The main advantages of this algorithm is first that it can efficiently deal with analysis-based regularization which is known to provide better results than synthesis-based priors. Second, this algorithm is highly flexible, as it can be used the same way for a large range of penalizations and the parameters that control its convergence speed are easier to tune than those involved in ADMM (aka, split Bregman) methods [48].

The experimental validation was made on prospectively collected ex vivo human brain data at 7 Tesla using different acquisition setups, i.e. various sampling patterns and acceleration factors. Image quality reaches a maximum for two regularization schemes, namely c-OSCAR and b-OSCAR penalties with a lower algorithmic complexity and so computational cost for the latter. A comparison with self-calibrating (ℓ_1-ESPIRiT)

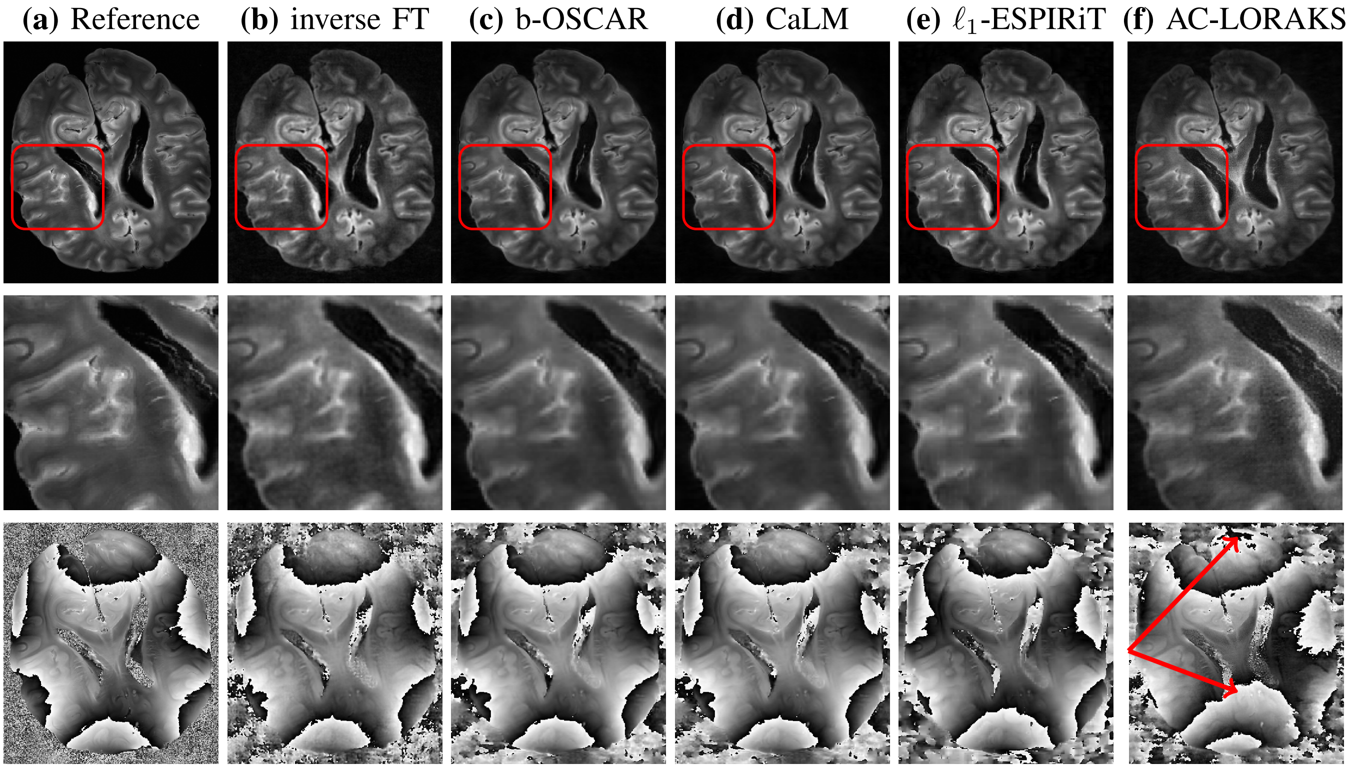

Fig. 3. **Top:** Reconstructed MR images (magnitude) from 20-fold accelerated Sparkling acquisitions using different methods. **(a)** Cartesian reference. **(b)** Reconstruction with no regularization term. **(c)** Reconstruction based on the subband-wise OSCAR formulation. **(d)** calibration-less reconstruction based on CaLM or group-LASSO regulatization. **(e)** Self-calibrating ℓ_1-ESPIRiT reconstruction. **(f)** Auto-calibrated (AC) LORAKS reconstruction. **Middle:** Respective zooms in the red square. Reconstructed MR images (phase). **Bottom:** Wrapped phase images extracted using the virtual coil approach.

and calibration-less (K-space based AC-LORAKS and wavelet based CaLM) methods was conducted. Quantitative structural similarity scores show that OSCAR-based approaches slightly improved the overall image quality with Sparkling and spiral trajectories compared to their competitors. On top of this improvement, phase information was better preserved for sparsity-based calibration-less reconstruction methods. This demonstrates the gain in robustness OSCAR-based reconstruction achieves compared to self-calibrating or gridded k-space based calibration-less techniques.

As for any regularized reconstruction approach, the performances of the proposed method depend on hyper-parameters. OSCAR penalization showed good stability over the setting of hyper-parameters, with a larger robustness range for λ compared to γ. In this work, both parameters have been set by maximizing the SSIM between a ground truth image reconstructed from a non-accelerated Cartesian acquisition and the image solution of Problem (1). Although this approach provided good results, it requires an additional lengthy Cartesian acquisition and leads to compare both different sampling schemes and reconstruction techniques. In the future, we will explore alternative automatic settings either based on (generalized) cross-validation [49] across slices for instance as a larger data set is necessary to implement this strategy, or on statistical inference (e.g. SURE estimator [49]), which requires the knowledge of noise statistics. The overall SSIM scores may also be improved using redundant wavelet transforms either considering undecimated decompositions or more sophisticated transforms such as Curvelet or Shearlet transforms [41], [50]. Although the aforementioned approaches might improve MR image quality for each reconstruction, it could also increase the computation time.

This work did not address the case of accelerated Cartesian acquisition and reconstruction. In this setup, the proposed approach can be useful as far as low acceleration factors are considered. However when acquisition is further shortened and the sampling kept over the Cartesian grid, the proposed calibration-less methodology – including CaLM and CLEAR methods – may perform worse than ℓ_1-ESPIRiT and AC-LORAKS. In that context, a fair self-calibrating approach would consist in solving regularized SENSE reconstruction combined with a OSCAR-norm regularization, thus extending the work done in [22].

The usual criticism of standard CS reconstruction methods is that they are highly computationally demanding compared to recent deep learning approaches. However, recently we have shown that online CS reconstruction is feasible in the single-channel receiver coil setup [51]. The main advantage of this algorithm is that it allows the physician to visualize the final reconstructed image by the end of acquisition. This is very appealing for making the clinical exam smoother compared to standard offline CS reconstruction techniques. The proposed calibration-less reconstruction framework may be ideal to extend this online technique to the parallel imaging setting

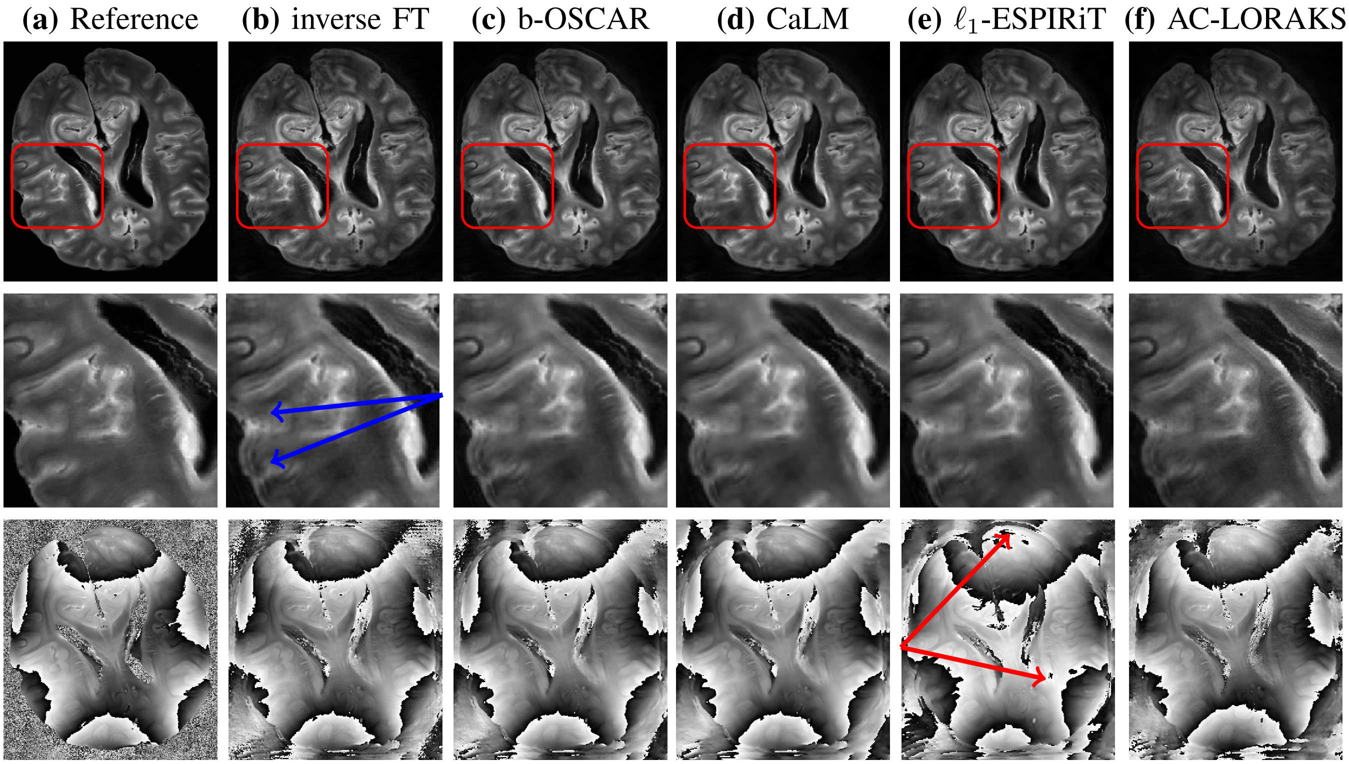

Fig. 4. **Top:** Reconstructed MR images (magntiude and phase) from 20-fold accelerated spiral acquisitions using different methods. **(a)** Cartesian reference. **(b)** Reconstruction with no regularization term. **(c)** Reconstruction based on the subband-wise OSCAR formulation. **(d)** calibration-less reconstruction based on CaLM or group-LASSO regulatization. **(e)** Self-calibrating ℓ_1-ESPIRiT reconstruction. **(f)** Auto-calibrated (AC) LORAKS reconstruction. **Middle:** Respective zooms in the red square. **Bottom:** Wrapped phase images extracted using the virtual coil approach. Off-resonance artifacts are shown by blue arrows on the inverse FT solution but remain present in all regularized reconstructions.

as it can run online reconstruction over multiple channels without any prior knowledge on the sensitivity maps. Also, both algorithms rely on the same primal-dual algorithm, hence this extension is quite straightforward.

The proposed method can be easily extended to 3D imaging and used as such in isotropic high-resolution susceptibility weighted imaging (SWI). In this context, the scan time is long and SWI acquisitions in clinical routine will benefit from non-Cartesian highly accelerated encoding schemes to reach 600 μm in 3 min. Noticeably, in SWI imaging, post-processing is applied to phase information in order to reveal potential alterations of the microvascular brain network. The fact that our calibration-less regularized reconstruction better preserves phase information is thus an asset for its utilization in SWI.

VI. CONCLUSIONS

In this paper, we have introduced a flexible regularized approach for solving the calibration-less MR image reconstruction inverse problem from highly accelerated and undersampled k-space data collected over a phased array of multiple receivers. On various prospective non-Cartesian acquisition setups at 7 Tesla, we have shown that OSCAR-norm regularization can achieve similar to better magnitude image quality without sensitivity map knowledge and preserve phase information more faithfully. In particular, subbandwise OSCAR-norm penalty reaches the best compromise between computational efficiency and image quality.

ACKNOWLEDGEMENTS

This research program was supported by a 2016 DRF Impulsion grant (COSMIC project, PI: P.C.) and a 2017 France Life Imaging grant (MultiCS-MRI, PI: P.C.). We would like to thank Prof. Jean-Christophe Pesquet (CentraleSupélec, France) for fruitful discussions and insightful comments. We are also grateful to Dr Samuel Farrens (CEA/CosmoStat) and Dr Antoine Grigis (CEA/NeuroSpin) for their help and support in the development of the PySAP software.

REFERENCES

[1] D. Donoho, “Compressed sensing,” *IEEE Transactions on Information Theory*, vol. 52, no. 4, pp. 1289–1306, 2006.
[2] E. Candès, J. Romberg, and T. Tao, “Robust uncertainty principles: Exact signal reconstruction from highly incomplete frequency information,” *IEEE Transactions on Information Theory*, vol. 52, no. 2, pp. 489–509, 2006.
[3] M. Lustig, D. Donoho, and J. Pauly, “Sparse MRI: The application of compressed sensing for rapid MR imaging,” *Magnetic Resonance in Medicine*, vol. 58, no. 6, pp. 1182–1195, 2007.
[4] “FDA Clears Compressed Sensing MRI Acceleration Technology From Siemens Healthineers,” https://www.siemens-healthineers.com/en-us/news/fda-clears-mri-technology-02-21-2017.html, accessed: 2019-04-15.
[5] J. G. Pipe, “Motion correction with PROPELLER MRI: application to head motion and free-breathing cardiac imaging,” *Magnetic Resonance in Medicine*, vol. 42, no. 5, pp. 963–969, 1999.
[6] J. H. Lee, B. A. Hargreaves, B. S. Hu, and D. G. Nishimura, “Fast 3d imaging using variable-density spiral trajectories with applications to limb perfusion,” *Magnetic Resonance in Medicine*, vol. 50, no. 6, pp. 1276–1285, 2003.

[7] L. Feng, L. Axel, H. Chandarana, K. T. Block, D. K. Sodickson, and R. Otazo, “Xd-grasp: golden-angle radial MRI with reconstruction of extra motion-state dimensions using compressed sensing,” *Magnetic Resonance in Medicine*, vol. 75, no. 2, pp. 775–788, 2016.

[8] C. Boyer, N. Chauffert, P. Ciuciu, J. Kahn, and P. Weiss, “On the generation of sampling schemes for magnetic resonance imaging,” *SIAM Journal on Imaging Sciences*, vol. 9, no. 4, pp. 2039–2072, 2016.

[9] L. Kasper, M. Engel, C. Barmet, M. Haeberlin, B. Wilm, B. Dietrich, T. Schmid, S. Gross, D. Brunner, K. Stephan *et al.*, “Rapid anatomical brain imaging using spiral acquisition and an expanded signal model,” *Neuroimage*, vol. 168, pp. 88–100, 2018.

[10] C. Lazarus, P. Weiss, N. Chauffert, F. Mauconduit, L. E. Gueddari, C. Destrieux, I. Zemmoura, A. Vignaud, and P. Ciuciu, “SPARKLING: variable-density kspace filling curves for accelerated T2*-weighted MRI,” *Magnetic Resonance in Medicine*, 2 2019.

[11] P. Roemer, W. Edelstein, C. Hayes, S. Souza, and O. Mueller, “The NMR phased array,” *Magnetic Resonance in Medicine*, vol. 16, no. 2, pp. 192–225, 1990.

[12] P. J. Shin, P. E. Larson, M. A. Ohliger, M. Elad, J. M. Pauly, D. B. Vigneron, and M. Lustig, “Calibrationless parallel imaging reconstruction based on structured low-rank matrix completion,” *Magnetic Resonance in Medicine*, vol. 72, no. 4, pp. 959–970, 2014.

[13] J. P. Haldar and J. Zhuo, “P-loraks: Low-rank modeling of local k-space neighborhoods with parallel imaging data,” *Magnetic Resonance in Medicine*, vol. 75, no. 4, pp. 1499–1514, 2016.

[14] M. Guerquin-Kern, M. Haberlin, K. P. Pruessmann, and M. Unser, “A fast wavelet-based reconstruction method for magnetic resonance imaging,” *IEEE transactions on medical imaging*, vol. 30, no. 9, pp. 1649–1660, 2011.

[15] L. Chaâri, J.-C. Pesquet, A. Benazza-Benyahia, and P. Ciuciu, “A wavelet-based regularized reconstruction algorithm for SENSE parallel MRI with applications to neuroimaging,” *Medical image analysis*, vol. 15, no. 2, pp. 185–201, 2011.

[16] L. Ying and J. Sheng, “Joint image reconstruction and sensitivity estimation in SENSE (JSENSE),” *Magnetic Resonance in Medicine*, vol. 57, no. 6, pp. 1196–1202, 2007.

[17] M. Uecker, P. Lai, M. Murphy, P. Virtue, M. Elad, J. Pauly, S. Vasanawala, and M. Lustig, “ESPIRiT– an eigenvalue approach to autocalibrating parallel MRI: where SENSE meets GRAPPA,” *Magnetic Resonance in Medicine*, vol. 71, no. 3, pp. 990–1001, 2014.

[18] L. Gueddari, C. Lazarus, H. Carrié, A. Vignaud, and P. Ciuciu, “Self-calibrating nonlinear reconstruction algorithms for variable density sampling and parallel reception MRI,” in *2018 IEEE 10th Sensor Array and Multichannel Signal Processing Workshop (SAM)*, 2018, pp. 415–419.

[19] L. Ying and J. Sheng, “Joint image reconstruction and sensitivity estimation in SENSE (JSENSE),” *Magnetic Resonance in Medicine*, vol. 57, no. 6, pp. 1196–1202, 2007.

[20] M. Uecker, T. Hohage, K. Block, and J. Frahm, “Image reconstruction by regularized nonlinear inversionjoint estimation of coil sensitivities and image content,” *Magnetic Resonance in Medicine*, vol. 60, no. 3, pp. 674–682, 2008.

[21] A. Majumdar and R. K. Ward, “Calibration-less multi-coil MR image reconstruction,” *Magnetic Resonance Imaging*, vol. 30, no. 7, pp. 1032–1045, 2012.

[22] I. Chun, B. Adcock, and T. Talavage, “Efficient compressed sensing SENSE pMRI reconstruction with joint sparsity promotion,” *IEEE Transactions on Medical Imaging*, vol. 35, no. 1, pp. 354–368, 2016.

[23] J. Trzasko and A. Manduca, “Calibrationless parallel MRI using CLEAR,” in *Signals, Systems and Computers (ASILOMAR), 2011 Conference Record of the Forty Fifth Asilomar Conference on*. IEEE, 2011, pp. 75–79.

[24] H. Bondell and B. Reich, “Simultaneous regression shrinkage, variable selection, and supervised clustering of predictors with OSCAR,” *Biometrics*, vol. 64, no. 1, pp. 115–123, 2008.

[25] M. Bogdan, E. Van Den Berg, C. Sabatti, W. Su, and E. J. Candès, “Slope-adaptive variable selection via convex optimization,” *The Annals of Applied Statistics*, vol. 9, no. 3, p. 1103, 2015.

[26] J.-J. Moreau, “Proximité et dualité dans un espace hilbertien,” *Bulletin de la Société mathématique de France*, vol. 93, pp. 273–299, 1965.

[27] L.-C. Man, J. M. Pauly, and A. Macovski, “Multifrequency interpolation for fast off-resonance correction,” *Magnetic Resonance in Medicine*, vol. 37, no. 5, pp. 785–792, 1997.

[28] J. Keiner, S. Kunis, and D. Potts, “Using NFFT 3—a software library for various nonequispaced fast fourier transforms,” *ACM Transactions on Mathematical Software (TOMS)*, vol. 36, no. 4, p. 19, 2009.

[29] J. Fessler and B. Sutton, “Nonuniform fast fourier transforms using min-max interpolation,” *IEEE Transactions on Signal Processing*, vol. 51, no. 2, pp. 560–574, Feb 2003.

[30] M. Elad, P. Milanfar, and R. Rubinstein, “Analysis versus synthesis in signal priors,” *Inverse problems*, vol. 23, no. 3, p. 947, 2007.

[31] A. Florescu, E. Chouzenoux, J.-C. Pesquet, P. Ciuciu, and S. Ciochina, “A majorize-minimize memory gradient method for complex-valued inverse problems,” *Signal Processing*, vol. 103, pp. 285–295, 2014.

[32] D. L. Parker, A. Payne, N. Todd, and J. R. Hadley, “Phase reconstruction from multiple coil data using a virtual reference coil,” *Magnetic Resonance in Medicine*, vol. 72, no. 2, pp. 563–569, 2014.

[33] L. Condat, “A primal–dual splitting method for convex optimization involving lipschitzian, proximable and linear composite terms,” *Journal of Optimization Theory and Applications*, vol. 158, no. 2, pp. 460–479, Aug 2013.

[34] B. Vũ, “A splitting algorithm for dual monotone inclusions involving cocoercive operators,” *Advances in Computational Mathematics*, vol. 38, no. 3, pp. 667–681, Apr 2013.

[35] P. L. Combettes and J.-C. Pesquet, “Proximal splitting methods in signal processing,” in *Fixed-point algorithms for inverse problems in science and engineering*. Springer, 2011, pp. 185–212.

[36] Z. X. and M. Figueiredo, “The ordered weighted l1 norm: Atomic formulation, projections, and algorithms,” *arXiv preprint arXiv:1409.4271*, 2014.

[37] P. Mair, K. Hornik, and J. de Leeuw, “Isotone optimization in r: pool-adjacent-violators algorithm (pava) and active set methods,” *Journal of Statistical Software*, vol. 32, no. 5, pp. 1–24, 2009.

[38] H. Zou and T. Hastie, “Regularization and variable selection via the elastic net,” *Journal of the royal statistical society: series B (statistical methodology)*, vol. 67, no. 2, pp. 301–320, 2005.

[39] A. Argyriou, R. Foygel, and N. Srebro, “Sparse prediction with the k-support norm,” in *Advances in Neural Information Processing Systems*, 2012, pp. 1457–1465.

[40] T. H. Kim, K. Setsompop, and J. P. Haldar, “Loraks makes better sense: Phase-constrained partial fourier sense reconstruction without phase calibration,” *Magnetic Resonance in Medicine*, vol. 77, no. 3, pp. 1021–1035, 2017.

[41] H. Cherkaoui, L. Gueddari, C. Lazarus, A. Grigis, F. Poupon, A. Vignaud, S. Farrens, J. Starck, and P. Ciuciu, “Analysis vs synthesis-based regularization for combined compressed sensing and parallel MRI reconstruction at 7 tesla,” in *26th European Signal Processing Conference (EUSIPCO 2018)*, 2018.

[42] Z. Wang, A. Bovik, H. Sheikh, and E. Simoncelli, “Image quality assessment: from error visibility to structural similarity,” *IEEE Transactions on Image Processing*, vol. 13, no. 4, pp. 600–612, 2004.

[43] M. A. Herráez, D. R. Burton, M. J. Lalor, and M. A. Gdeisat, “Fast two-dimensional phase-unwrapping algorithm based on sorting by reliability following a noncontinuous path,” *Applied Optics*, vol. 41, no. 35, pp. 7437–7444, 2002.

[44] J. P. Haldar, “Autocalibrated loraks for fast constrained mri reconstruction,” in *2015 IEEE 12th International Symposium on Biomedical Imaging (ISBI)*. IEEE, 2015, pp. 910–913.

[45] B. Zhu, J. Z. Liu, S. F. Cauley, B. R. Rosen, and M. S. Rosen, “Image reconstruction by domain-transform manifold learning,” *Nature*, vol. 555, no. 7697, p. 487, 2018.

[46] M. Mardani, E. Gong, J. Y. Cheng, S. S. Vasanawala, G. Zaharchuk, L. Xing, and J. M. Pauly, “Deep generative adversarial neural networks for compressive sensing MRI,” *IEEE Transactions on Medical Imaging*, vol. 38, no. 1, pp. 167–179, 2018.

[47] V. Antun, F. Renna, C. Poon, B. Adcock, and A. C. Hansen, “On instabilities of deep learning in image reconstruction-does ai come at a cost?” *arXiv preprint arXiv:1902.05300*, 2019.

[48] S. Ramani and J. A. Fessler, “Parallel MR image reconstruction using augmented lagrangian methods,” *IEEE Transactions on Medical Imaging*, vol. 30, no. 3, pp. 694–706, 2010.

[49] S. Ramani, Z. Liu, J. Rosen, J.-F. Nielsen, and J. A. Fessler, “Regularization parameter selection for nonlinear iterative image restoration and mri reconstruction using GCV and SURE-based methods,” *IEEE Transactions on Image Processing*, vol. 21, no. 8, pp. 3659–3672, 2012.

[50] J. Ma, “Generalized sampling reconstruction from Fourier measurements using compactly supported shearlets,” *Applied and Computational Harmonic Analysis*, vol. 42, no. 2, pp. 294–318, 2017.

[51] L. El Gueddari, E. Chouzenoux, J.-C. Pesquet, A. Vignaud, and P. Ciuciu, “Online compressed sensing MR image reconstruction for high resolution T_2^* imaging,” in *27th*, no. 4655, Montreal, QC, Canada, May 2019.